11th International Symposium on Turbulence and Shear Flow Phenomena (TSFP11)
Southampton, UK, July 30 to August 2, 2019

INFLUENCE OF AIRFOIL SHAPE ON ACTIVE DRAG REDUCTION EFFICIENCY

Marian Albers
Institute of Aerodynamics
RWTH Aachen University
Wüllnerstraße 5a, 52062 Aachen
m.albers@aia.rwth-aachen.de

Pascal S. Meysonnat
Institute of Aerodynamics
RWTH Aachen University
Wüllnerstraße 5a, 52062 Aachen
p.meysonnat@aia.rwth-aachen.de

Wolfgang Schröder
Institute of Aerodynamics
RWTH Aachen University
Wüllnerstraße 5a, 52062 Aachen

JARA Center for Simulation and Data Sciences
RWTH Aachen University
Seffenter Weg 23, 52074 Aachen
office@aia.rwth-aachen.de

1 ABSTRACT

Active flow control of the turbulent flow over two airfoils of different shape is performed with the goal of increasing the overall aerodynamic efficiency. Large-eddy simulations are performed to investigate the impact of spanwise traveling transversal surface waves which are applied to a large percentage of the suction and the pressure side of the DRA2303 and NACA4412 airfoils at a chord based Reynolds number of $\mathrm{Re}_c = 400,000$. The results show a substantial decrease of the total integrated drag together with a slight increase of the lift. A detailed analysis reveals a decrease of the turbulent stresses and an attenuation of the boundary layer growth, resulting in an improvement of the lift-drag ratio for both airfoils.

2 INTRODUCTION

Increasing energy efficiency in air travel is one of the keys to reduce global CO_2 emissions. Furthermore, even savings on the order of one percent in fuel consumption can be decisive in the competition between aircraft manufacturers and have a vast impact on airline economics. The drag of slender bodies moving in a fluid at high Reynolds numbers, e.g., aircraft in cruise flight, is to a large part determined by viscous friction, most often due to turbulent boundary layers developing around the wings and the fuselage. Therefore, reducing this friction drag has been of interest for the past decades. Drag reduction techniques can be classified by whether or not additional energy is introduced into the system. A further classification is possible by considering techniques which delay or prevent transition from laminar to turbulent flow and techniques which alter the state of an already turbulent boundary layer, thereby reducing the viscous drag.

Among passive techniques, i.e., without the input of external energy, the best known approach is streamwise aligned surface protrusions, so-called riblets, which have proven to reduce friction drag in experimental (Bechert *et al.*, 1997) and numerical setups (García-Mayoral & Jiménez, 2011). Moreover, they are one of the few technologies that have demonstrated to work on real aircraft in flight conditions (Walsh *et al.*, 1989). Other passive techniques include compliant coatings (Choi *et al.*, 1997) and superhydrophobic surfaces (Gose *et al.*, 2018).

Active techniques, which require the introduction of external energy into the system, have the advantage of flexiblity of the control parameters, enabling an adjustment of the control to varying operating conditions. An extensive overview of active in-plane drag reduction techniques is given by Quadrio (2011). Methods like spanwise oscillating walls (Jung *et al.*, 1992) and streamwise traveling waves of spanwise wall velocity (Quadrio *et al.*, 2009) are to be mentioned in this context. In general, these relatively new techniques have been investigated solely in canonical flow setups, e.g., Poisseuille flow and zero-pressure gradient turbulent boundary layer flow. Nevertheless, they are attractive due to the large drag reduction possible and the substantial attentuation of turbulent motion.

Most of the aforementioned methods, both passive and active, focus on reducing viscous drag in turbulent boundary layers. Many more techniques are available for bluff body flow control (Choi *et al.*, 2008), i.e., control of the total drag of a body consisting of pressure and viscous drag. That is, a more global perspective needs to be taken into account, as the reduction of viscous drag might result in pressure penalties and vice versa (Spalart & McLean, 2011). A reduction of the skin friction on airfoils using, for instance, steady blowing can result in a thickening of the boundary layer, causing additional pressure drag from the wake, whereas the opposite can happen for steady suction

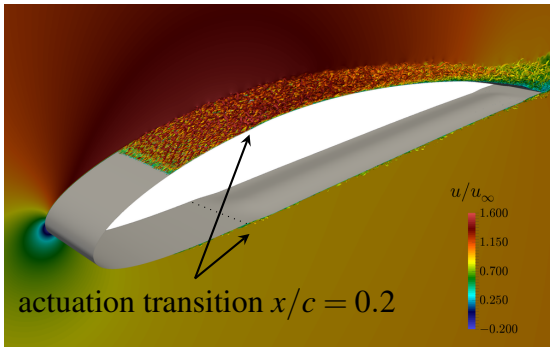

Figure 1: Contours of the λ_2-criterion of the instantaneous velocity field of the actuated NACA4412 airfoil colored by the instantaneous streamwise velocity.

(Atzori *et al.*, 2018). Hence, a drag reduction technique is desirable which reduces friction drag while also preventing boundary layer growth, as has been shown for instance for body force control (Stroh *et al.*, 2016). Another promising technique enabling such a favorable combination is spanwise traveling transversal surface waves for which a coupled decrease of pressure and viscous drag has been shown for airfoil flow (Albers *et al.*, 2019). We extend this study by considering another airfoil with a distinctively different geometry. A comparison between the effects of the drag reduction method on the flow over the two airfoils is presented to substantiate the applicability of the spanwise-traveling-wave approach to turbulent flow around slender bodies.

3 NUMERICAL METHOD

The numerical method is a high resolution large-eddy simulation (LES) solving the filtered compressible unsteady Navier-Stokes equation on curvilinear grids. For the convective fluxes, the advection upstream splitting method (AUSM) is used, while a central scheme is employed for the viscous terms. The temporal integration is performed by an explicit 5-stage Runge-Kutta method of second-order accuracy. An implicit LES model is used, following the approach of monotonically integrated LES (MILES) by Boris *et al.* (1992) such that the AUSM provides for the necessary dissipation for the smallest scales. Investigations by Meinke *et al.* (2002) have shown that no additional explicit turbulence model is required. The code has been used and verified for a wide range of flow problems, including turbulent boundary layer flow over moving surfaces (Klumpp *et al.*, 2010b) and turbulent airfoil flow (Albers *et al.*, 2019).

4 COMPUTATIONAL SETUP

We compare the impact of a surface actuation technique on the flow field over two airfoils. The first geometry is a DRA2303 airfoil, designed for transonic flow (Fulker & Simmons, 1997), with a maximum thickness of 14 percent chord. The findings for this configuration are already discussed in detail in Albers *et al.* (2019). The second configuration is a NACA4412 airfoil, for which extensive DNS and LES studies exist (Hosseini *et al.*, 2016; Vinuesa *et al.*, 2018) and also drag reduction setups have been analyzed (Atzori *et al.* (2018)).

The flow around the airfoil is defined in a Cartesian domain defined by $\mathbf{x} = (x, y, z)$ and the corresponding flow velocities are denoted by $\mathbf{u} = (u, v, w)$. The chord of the airfoil is aligned with the x-axis and the spanwise coordinate is z. Periodicity in the spanwise direction is enforced to obtain an infinite span. The density is given by ρ and the pressure is denoted by p. The flow is described by the unsteady compressible Navier-Stokes equation. The physical domain has an extent of 50 chords in the x- and y-direction and a width of 10 percent chord which is sufficient to resolve the largest turbulent scales (Hosseini *et al.*, 2016). A C-type curvilinear mesh is used to discretize the physical domain, the resolution in the wall-normal direction in the very near-wall region is $\Delta y^+|_{wall} < 1.6$ on the suction side and $\Delta y^+|_{wall} < 1.0$ on the pressure side with gradual coarsening off the wall. The resolution is $\Delta x^+ < 23.0$ in the wall-tangential direction and $\Delta z^+ < 9.0$ in the spanwise direction. An angle of attack of $\alpha = 5.0^\circ$ for the NACA airfoil and $\alpha = 2.0^\circ$ for the DRA airfoil is prescribed by adjusting the velocity vector of the incoming flow. A numerical tripping (Schlatter & Örlü, 2012) at $x/c = 0.1$ on both sides of the airfoil triggers laminar-turbulent transition. The Reynolds number based on the chord length c is $\mathrm{Re}_c = u_\infty c/\nu = 400,000$ sucht that friction Reynolds numbers of up to $\mathrm{Re}_\tau = u_\tau \delta_{99}/\nu \approx 400$ are achieved. The Mach number is $\mathrm{M} = 0.1$.

A space- and time-dependent function

$$y_n^+|_{\mathrm{wall}}(x, z^+, t^+) = A^+(x) \cos\left(\frac{2\pi}{\lambda^+} z^+ - \frac{2\pi}{T^+} t^+\right) \quad (1)$$

is applied to the airfoil surface in the interval $x/c \in [0.2, 0.95]$ on the pressure and suction side to generate a sinusoidal deflection of the solid wall in the wall-normal direction traveling in the spanwise direction. Smooth transitions from a non-actuated to an actuated wall and vice-versa are achieved via $1 - \cos(x)$ functions in the intervals $x/c \in [0.2, 0.25]$ and $x/c \in [0.9, 0.95]$. An illustration of the airfoil and the positions of the onset of the actuation is given in Fig. 1. The distributions of the parameters of the traveling wave function in inner scaling, i.e., the amplitude A^+, the wavelength λ^+, and the period T^+, non-dimensionalized by local values of u_τ, are shown in Fig.2. A general difficulty in defining a reasonable distribution of the wave parameters is the strongly varying friction velocity along the airfoil chords, especially on the suction side of the NACA airfoil. Therefore, the parameters are chosen to lie in an interval whose bounds are relevant for the current airfoil flow. Based on the knowledge from previous studies the period is kept around a value of $T^+ \approx \mathcal{O}(50)$ (cf. Fig. 2b) and the wavelength is chosen as large as possible, i.e., one wavelength over the whole domain width. A near constant distribution of the amplitude in inner units (cf. Fig. 2c) for the NACA airfoil is achieved by a linear increase of the amplitude in outer scales (cf. Fig. 2d) along the chord on the suction side, on the pressure side a constant value is already adequate. In this regard, the NACA airfoil shows a favorable distribution of the skin-friction, being nearly constant on the pressure side and following a linear decrease on the suction side. In contrast, the distributions around the DRA airfoil create a more challenging situation such that a linear function for the increase of the amplitude in outer scaling does not result in a near-constant distribution in inner scales (cf. Fig. 2d).

Details about the simulation procedure for the DRA airfoil can be found in Albers *et al.* (2019), the simulations for the NACA airfoil are conducted as follows. First, the non-actuated reference setup is run for $tu_\infty/c \approx 24.0$ flow-over times until quasi-steady distributions of the lift

and the drag are observed. Then, flow statistics were collected for $tu_\infty/c \approx 7$ flow-over times. Subsequently, the actuated setup is initialized with a converged flow field of the non-actuated reference case and the transition between solid wall and actuated wall is initiated. Once a quasi-steady state is observed statistics are gathered for the actuated flow.

5 RESULTS

Detailed results on the actuated flow around the DRA2303 airfoil are discussed in Albers *et al.* (2019). Therefore, statistics from this setup are shown primarily for a comparison with the new results on the NACA4412 airfoil, which we focus on in this study.

An illustration of the actuated flow field of the NACA4412 case is given in Fig. 1. However, no direct conclusion can be derived from the image since the majority of the flow modulation due to the control is confined to the near-wall region. Temporal distributions of the overall drag coefficient c_d, viscous drag coefficient $c_{d,v}$, and lift coefficient c_l for the NACA4412 airfoil are depicted in Fig. 3. Note that all distributions are normalized by the temporal average of the corresponding coefficient of the non-actuated reference case. Similar to the observations in Albers *et al.* (2019), the viscous drag is directly affected after the initialization of the actuation and an averaged decrease of 12.9 percent is measured. For the DRA2303 case a decrease of 8.6 was achieved. The total drag (cf. Fig. 3b), i.e., the pressure contribution plus the viscous drag, shows the same tendency of being rapidly decreased. On average, it is 8.5 percent lower compared to the non-actuated reference case, which can be largely attributed to the decrease of the viscous part, whereas the pressure drag is modified by only 3.1 percent. The short time scale on which the modification of the integrated viscous drag takes place can be explained by the quick development of a periodically fluctuating secondary flow field with wall-normal and spanwise flow velocities above the traveling wave. This flow, resembling a directed oscillating Stokes layer with oscillating fluid instead of an oscillating plate, has an almost immediate effect, i.e., within few periods of the motion (Touber & Leschziner (2012)), on the turbulent structures, especially near the wall. A somewhat larger time scale is apparent for the modification of the lift (cf. Fig. 3c) which is mainly determined by the pressure distribution. Only after about $tu_\infty/c \approx 0.5-1.0$ flow-over times a departure from the distribution of the non-actuated reference case becomes apparent and a new quasi-steady state is reached not before $tu_\infty/c \approx 4.0$ flow-over times after the onset of the actuation. A similar behavior was observed for the DRA2303 induced through the modified boundary layer and its decreased thickness, altering the flow over the trailing edge and in the wake region and thereby having a delayed effect on the overall pressure distribution. However, it is important to note that on average an increase of the lift by 1.4 percent is obtained. In combination with the lowered overall drag, this leads to an increase of the aerodynamic efficiency L/D by 10.8 percent. An overview of all alterations of the aerodynamic coefficients of both airfoils is given in Tab. 1.

The detailed changes of the skin-friction coefficient c_f are presented in Fig. 4 for the suction and the pressure side. On the suction side of both airfoils, the bulk of the skin-friction decrease is achieved in the forward part of the airfoil, i.e., $x/c < 0.5$, whereas further downstream the effect of the traveling wave actuation is steadily decreasing. This

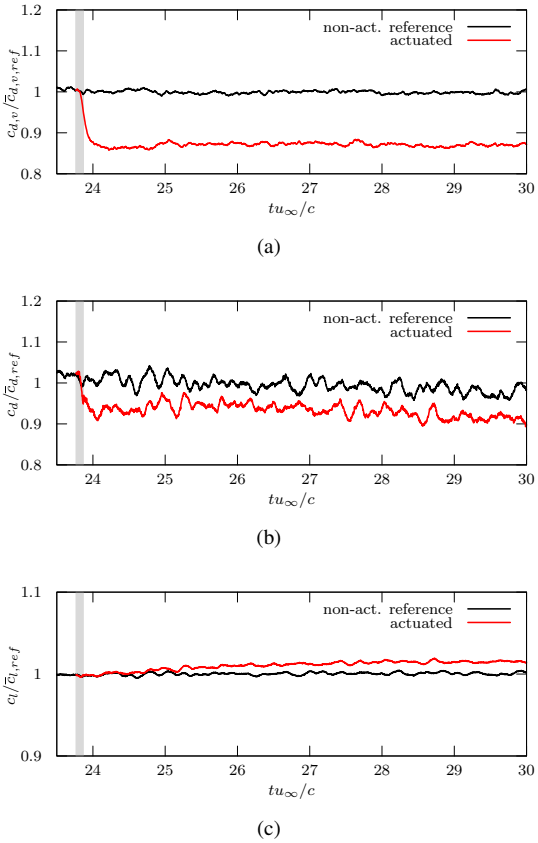

Figure 3: Temporal distribution of (a) the viscous drag, (b) the total drag, and (c) the total lift of the NACA4412 airfoil of the non-actuated reference case and the actuated case, both normalized by the averaged coefficients of the non-actuated reference case.

Case	Δc_d	$\Delta c_{d,v}$	$\Delta c_{d,p}$	Δc_l	$\Delta(L/D)$	ΔA_s
NACA	8.5	12.9	3.1	-1.4	-10.8	-0.5
DRA	7.5	8.6	5.0	-1.4	-9.6	-1.6

Table 1: Overview of the change of the aerodynamic coefficients in percent of the two airfoils by the traveling wave actuation, negative values indicate an increase.

effect is a combination of a reduced efficiency of the control due to the increasing thickness-based Reynolds number of the boundary layer (Gatti & Quadrio (2016)) and non-ideal control parameters. Especially the period T, which is constant in outer scaling, is in an efficient range only in a subdomain of the whole streamwise extent of the actuation. On the pressure side of the NACA airfoil, the skin-friction reduction shows a more constant distribution, with a considerable decrease even around $x/c \approx 0.9$. This advantageous behavior can be attributed to the much slower growth of the boundary layer, compared to the suction side, and a nearly constant skin-friction distribution in the reference case. Therefore, the values of the control parameters are in an effective interval over the whole extent of the actuated pressure side. In contrast, the skin-friction distribution on the pressure side of the DRA airfoil shows a decrease simi-

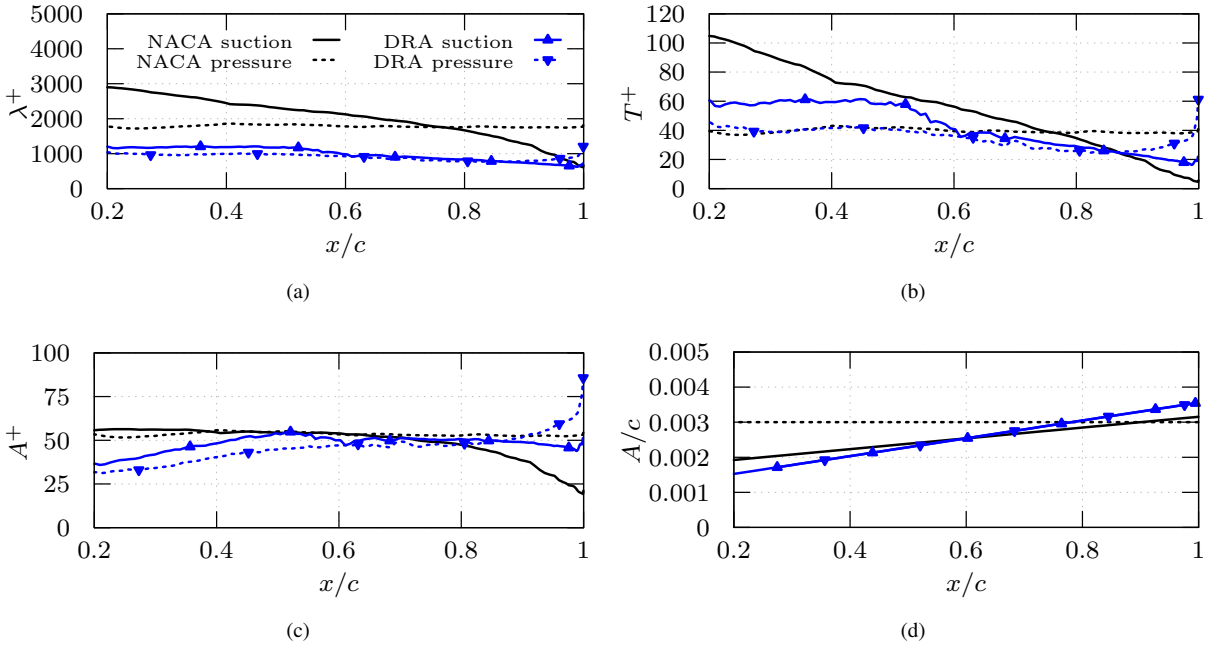

Figure 2: Traveling transversal wave parameters (a) wavelength, (b) period, and (c) amplitude in inner scaling, and (d) amplitude in outer scaling.

lar to the suction side, thus a reduced impact of the actuation can be expected.

A combined analysis of the skin-friction distribution (cf. Fig. 4) together with the momentum thickness distribution shown in Fig. 5 reveals an advantageous feature of this type of flow control. While the skin-friction distribution downstream of the end of the control region quickly recovers and approaches the non-actuated reference state, a persisting effect is evident in the momentum thickness. The decreased thickness of the actuated boundary layer holds till the trailing edge, resulting in the increased lift and the decreased pressure drag.

To obtain a high overall drag reduction, the streamwise extension of the control region is to be maximized otherwise a skin friction increase due to the decrease of the boundary layer thickness downstream of the control region, as described by Stroh *et al.* (2016), deteriorates the global measured drag. Therefore, unlike for drag reduction investigations for canonical flows, such as turbulent channel flow or zero pressure gradient turbulent boundary layer flow, multiple additional factors contributing to the total aerodynamic efficiency have to be considered. A global perspective is necessary when evaluating the applicability of any drag reduction method to an airfoil (Spalart & McLean, 2011). A closer look at the second-order moments of the velocity and the vorticity is taken in the following. The turbulent velocity fluctuations across the boundary layer height for both airfoils are compared in Fig. 6 on the suction side at the chordwise position $x/c = 0.5$, which corresponds to a friction Reynolds number of $Re_\tau = 312$ for the NACA airfoil and $Re_\tau = 269$ for the DRA airfoil. Although the Reynolds number and the strength of the fluctuations is different at the same streamwise location, the effect of the control is similar. Reductions of all four components are apparent throughout the whole boundary layer. The reductions of the wall-tangential fluctutations are most pronounced. Due to the exceptionally strong attenuation in the near-wall region, i.e., $y^+ < 15$, a direct effect of the actuation on the

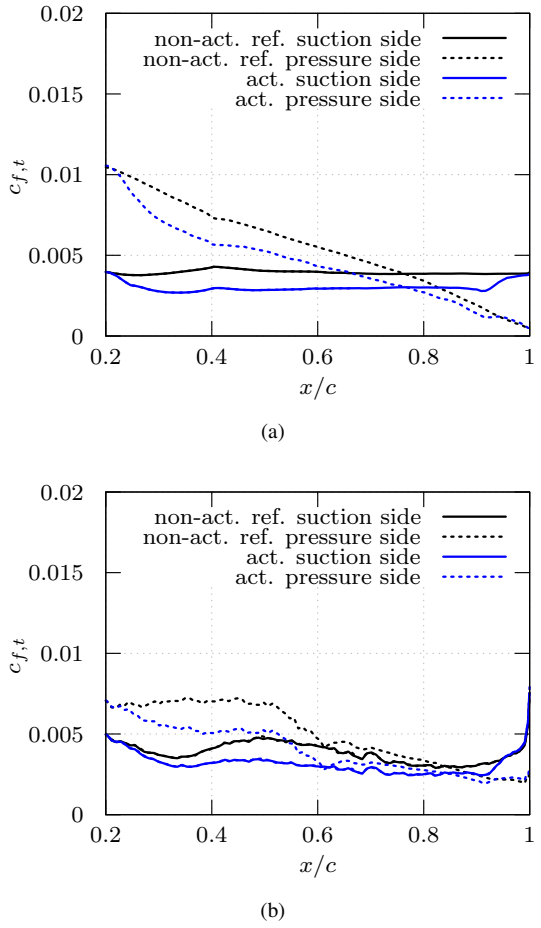

Figure 4: Temporal and spanwise average of the wall-tangential skin-friction coefficient $c_{f,t}$ of (a) the NACA4412 cases and (b) the DRA2303 cases.

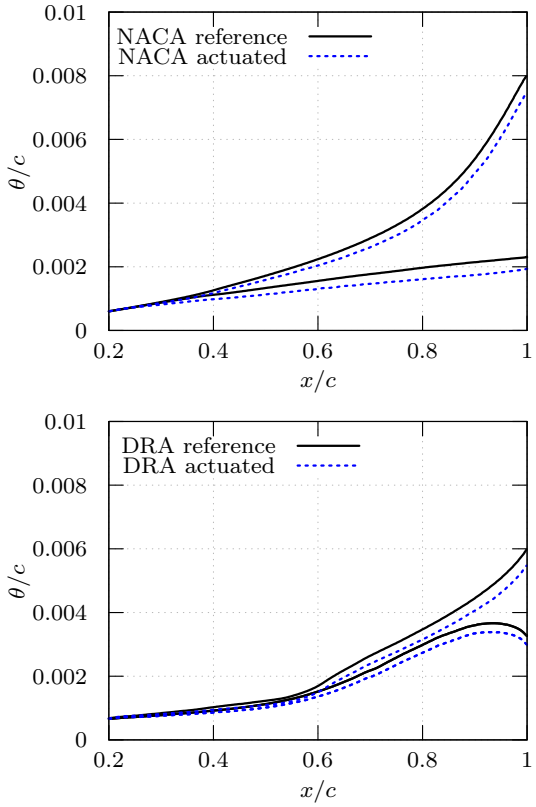

Figure 5: Temporal and spanwise average of the momentum thickness θ of (a) the NACA4412 cases and (b) the DRA2303 cases.

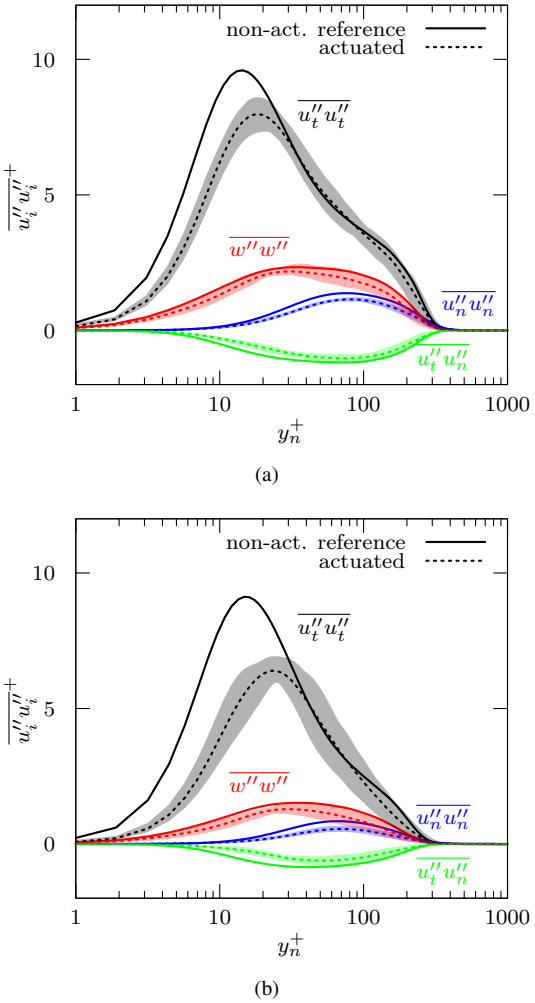

Figure 6: Wall-normal distributions of the symmetric and the shear-stress components of the Reynolds stress tensor at $x/c = 0.5$ of (a) the NACA4412 cases and (b) the DRA2303 cases, normalized by the friction velocity of the non-actuated reference case. The shaded regions illustrate phasewise variations of the depicted quantity.

near-wall streaks can be suspected, similar to spanwise oscillating wall (Touber & Leschziner, 2012). Furthermore, the strong decrease of the shear stress, in relative terms, near the wall contributes strongly to the decrease of the skin friction.

This direct interference of the oscillating secondary flow field with the near-wall streaks, in opposition to quasi-streamwise vortices, is corroborated by the distributions of the averaged vorticity fluctuations depicted in Fig. 7. The wall-normal and spanwise vorticity fluctuations close to the wall, which are typically associated with near-wall streaks, are considerably damped. However, there is almost no variation of the wall-tangential component, which would evidence the existence of quasi-streamwise vortices.

6 CONCLUSION

Large-eddy simulations of turbulent airfoil flow for two airfoil shapes were conducted. The flow control method of spanwise traveling transversal surface waves was applied to the suction and the pressure side of a DRA2303 and of a NAC4412 wing section. The parameters of the time- and space-dependent actuation function were adjusted to be in an efficient range in inner scaling using the local skin-friction.

The results show a general decrease of the integrated viscous drag for both airfoils and also a slight reduction of the pressure drag. In combination with an increase of the lift, owing to a reduced boundary layer thickness at the trailing edge, the aerodynamic efficiency is improved for both airfoil shapes. Based on the current findings it can be stated that, the flow control technique - spanwise transversal surface waves - yields highly promising aerodynamic results for massively different airfoil shapes. Nevertheless, it has to be kept in mind that the airfoil shape and the developing boundary layers require to calibrate the control parameters of the actuation system, especially when a large percentage of the airfoil surface is subject to the control. Although the findings of this study are very promising with respect to active flow control and drag reduction, there is still lots of research to be done, i.e., higher Reynolds number flows, compressible flows, etc. are to be analyzed, to assess whether or not drag reduction can be achieved in cruise flight.

ACKNOWLEDGMENT

The research was funded by the Deutsche Forschungsgemeinschaft (DFG) in the framework of the research projects SCHR 309/52 and SCHR 309/68. The authors gratefully acknowledge the Gauss Centre for Supercomputing e.V. (www.gauss-centre.eu) for funding this project by providing computing time on the GCS Supercomputers

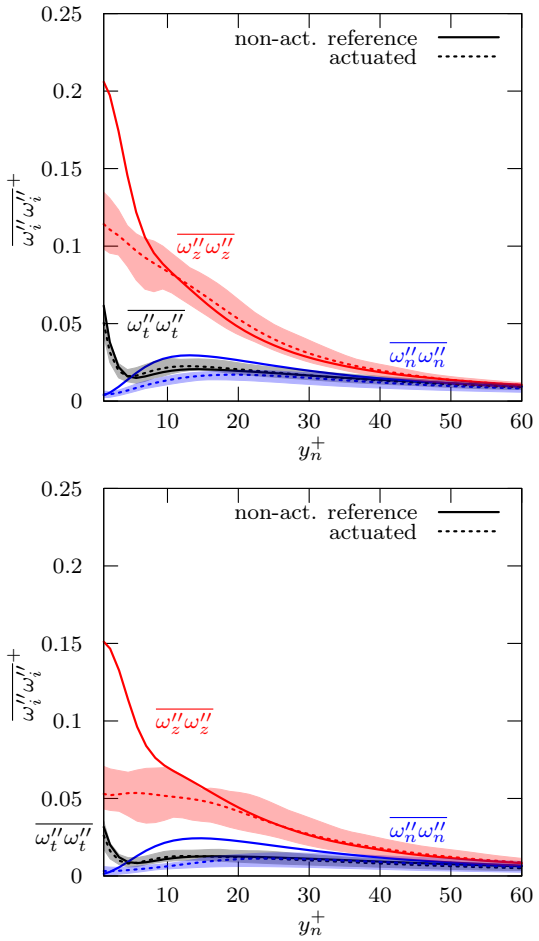

Figure 7: Wall-normal distributions of the averaged vorticity fluctuations at $x/c = 0.5$ of (a) the NACA4412 cases and (b) the DRA2303 cases, normalized by the friction velocity of the non-actuated reference case. The shaded regions illustrate phase-wise variations of the depicted quantity.

Hazelhen at HLRS Stuttgart and JURECA at Jülich Supercomputing Centre (JSC).

REFERENCES

Albers, M., Meysonnat, P. S. & Schröder, W. 2019 Actively reduced airfoil drag by transversal surface waves. *Flow Turbul. Combust.* **102** (4), 865–886.

Atzori, M., Vinuesa, R., Stroh, A., Frohnapfel, B. & Schlatter, P. 2018 Assessment of skin-friction-reduction techniques on a turbulent wing section. In *12th ERCOFTAC Symp. on Engineering Turbulence Modeling and Measurements (ETMM12)*.

Bechert, D. W., Bruse, M., Hage, W., Hoeven, J. G. T. Van Der & Hoppe, G. 1997 Experiments on drag-reducing surfaces and their optimization with an adjustable geometry. *J. Fluid Mech.* **338**, 59–87.

Boris, J. P., Grinstein, F. F., Oran, E. S. & Kolbe, R. L. 1992 New insights into large eddy simulation. *Fluid Dyn. Res.* **10** (4-6), 199–228.

Choi, H., Jeon, W.-P. & Kim, J. 2008 Control of flow over a bluff body. *Annu. Rev. Fluid Mech.* **40** (1), 113–139.

Choi, K.–S., Yang, X., Clayton, B. R., Glover, E. J., Atlar, M., Semenov, B. N. & Kulik, V. M. 1997 Turbulent drag reduction using compliant surfaces. *Proc. R. Soc. London, Ser. A* **453** (1965), 2229–2240.

Fulker, J. L. & Simmons, M. J. 1997 *An Experimental Investigation of Passive Shock/Boundary-Layer Control on an Aerofoil*, pp. 379–400. Wiesbaden: Vieweg+Teubner Verlag.

García-Mayoral, R. & Jiménez, J. 2011 Drag reduction by riblets. *Philos. Trans. R. Soc. London, Ser. A* **369** (1940), 1412–1427.

Gatti, D. & Quadrio, M. 2016 Reynolds-number dependence of turbulent skin-friction drag reduction induced by spanwise forcing. *J. Fluid Mech.* **802**, 553–582.

Gose, J. W., Golovin, K., Boban, M., Mabry, J. M., Tuteja, A., Perlin, M. & Ceccio, S. L. 2018 Characterization of superhydrophobic surfaces for drag reduction in turbulent flow. *J. Fluid Mech.* **845**, 560–580.

Hosseini, S. M., Vinuesa, R., Schlatter, P., Hanifi, A. & Henningson, D. S. 2016 Direct numerical simulation of the flow around a wing section at moderate Reynolds number. *Int. J. Heat Fluid Flow* **61**, 117–128.

Jung, W. J., Mangiavacchi, N. & Akhavan, R. 1992 Suppression of turbulence in wallbounded flows by high-frequency spanwise oscillations. *Phys. Fluids A* **4** (8), 1605–1607.

Klumpp, S., Meinke, M. & Schröder, W. 2010b Drag reduction by spanwise transversal surface waves. *J. Turbul.* **11**.

Meinke, M., Schröder, W., Krause, E. & Rister, Th. 2002 A comparison of second- and sixth-order methods for large-eddy simulations. *Comput. Fluids* **31** (4), 695–718.

Quadrio, M. 2011 Drag reduction in turbulent boundary layers by in-plane wall motion. *Philos. Trans. R. Soc. London, Ser. A* **369** (1940), 1428–1442.

Quadrio, M., Ricco, P. & Viotti, C. 2009 Streamwise-travelling waves of spanwise wall velocity for turbulent drag reduction. *J. Fluid Mech.* **627**, 161.

Schlatter, P. & Örlü, R. 2012 Turbulent boundary layers at moderate Reynolds numbers: inflow length and tripping effects. *J. Fluid Mech.* **710**, 5–34.

Spalart, P. R. & McLean, J. D. 2011 Drag reduction: enticing turbulence, and then an industry. *Philos. Trans. R. Soc. London, Ser. A* **369** (1940), 1556–1569.

Stroh, A., Hasegawa, Y., Schlatter, P. & Frohnapfel, B. 2016 Global effect of local skin friction drag reduction in spatially developing turbulent boundary layer. *J. Fluid Mech.* **805**, 303321.

Touber, E. & Leschziner, M. A. 2012 Near-wall streak modification by spanwise oscillatory wall motion and drag-reduction mechanisms. *J. Fluid Mech.* **693**, 150–200.

Vinuesa, R., Negi, P. S., Atzori, M., Hanifi, A., Henningson, D. S. & Schlatter, P. 2018 Turbulent boundary layers around wing sections up to $Re_c = 1,000,000$. *Int. J. Heat Fluid Flow* **72**, 86–99.

Walsh, M. J., Sellers III, W. L. & Mcginley, C. B. 1989 Riblet drag at flight conditions. *J. Aircraft* **26** (6), 570–575.